12-μm-Pitch Electromechanical Resonator for Thermal Sensing

Ludovic Laurent,[1,2] Jean-Jacques Yon,[1,2] Jean-Sébastien Moulet,[1,2] Michael Roukes,[3] and Laurent Duraffourg[1,2,*]
[1]*Université Grenoble Alpes, F-38000 Grenoble, France*
[2]*CEA, LETI, Minatec Campus, F-38054 Grenoble, France*
[3]*Departments of Physics, Applied Physics, and Bioengineering, Kavli Nanoscience Institute, California Institute of Technology, MC 149-33, Pasadena, California 91125, USA*

(Received 24 May 2017; revised manuscript received 28 August 2017; published 15 February 2018)

We provide here a demonstration of 12-μm-pitch nanoelectromechanical resonant infrared sensors with fully integrated capacitive transduction. A low-temperature fabrication process is used to manufacture torsional resonator arrays. An H-shaped pixel with 9-μm-long nanorods and (250×30)-nm^2 cross section is designed to provide high thermal response whose experimental measurements reach up to 1024 Hz/nW. A mechanical dynamic range of over 113 dB is obtained, which leads to an Allan deviation of $\sigma_A = 3 \times 10^{-7}$ at room temperature and 50-Hz noise bandwidth ($\sigma_A = 1.5 \times 10^{-7}$ over 10 Hz). These features allow us to reach a sensitivity of (8–12)-μm radiation of 27 pW/$\sqrt{\mathrm{Hz}}$ leading to a noise-equivalent temperature difference (NETD) of 2 K for a 50-Hz noise bandwidth (NETD = 1.5 K at 10 Hz). We demonstrate that the resolution is no more set by the phonon noise but by the anomalous phase noise already encountered in flexural nanoresonators. By both improving the temperature coefficient of frequency of a factor 10 and using a readout electronics at the pixel level, these resonators will lead to a breakthrough for uncooled infrared detectors. We expect that the NETD will rapidly drop to 180 mK with electronics close to the pixel. As a result of the features of our torsional resonators, an alternative readout scheme of pixels is suggested.

DOI: 10.1103/PhysRevApplied.9.024016

I. INTRODUCTION

Over the last 20 years, infrared focal plane arrays (IRFPAs) with large pixel count have emerged as the keystone of modern thermal imaging systems which are becoming widely used for night vision, thermography, surveillance, firefighting, and driving assistance. In the field of infrared imaging, there are two main categories of infrared detectors, namely, quantum detectors and thermal detectors. Quantum detectors can provide very high performance but require operation at cryogenic temperature to minimize the dark current. On the contrary, thermal detectors operate at room temperature but feature lower performance. The advantage of the absence of the cooling system has given thermal detectors an edge that can largely counterbalance the lower performance in many commercial applications requiring the availability of affordable low-power small-size handheld thermal cameras. Among the various possible uncooled IRFPA technologies, the microbolometer has become the most prominent uncooled infrared technology. Microbolometers operate by converting the heating of a thin membrane induced by the IR absorption in a variation of electrical resistance. The sensitive part of a microbolometer pixel acts as a thermistor. These thermistors are commonly made of a semiconductor thin film, using mostly vanadium oxide (VO_x) or amorphous silicon (a-Si) because of their high thermal sensitivity ($1/R \times dR/dT$), about 2%–3%/K.

The induced heating effect of the thermistor is advantageously enhanced by achieving a high thermal insulation between the sensor and the substrate. The thermal insulation is commonly achieved with thin and long insulation legs, which support the sensitive part of the sensor suspended above the readout integrated circuit (ROIC). Thermal insulation as high as 2 MK/W has been reported for microbolometers with 12-μm pixel pitch [1]. This development has paved the way for further cost reduction of uncooled infrared cameras while keeping the noise-equivalent temperature differences (NETDs) at a very low level, around 50 mK ($f/1$ lens, 30-Hz frame rate, 300-K background) [2,3].

Because of the high thermal insulation, the temperature of the sensing material can increase dramatically in the case of excessive radiant power exposures,

*Corresponding author.
laurent.duraffourg@cea.fr

 © 2018 American Physical Society

leading to a detrimental drift of the thermistor properties. First of all, the resistivity of the sensing material can be altered. This effect is reported to be linked with a temperature-induced crystallographic transformation of the sensing material resulting in a significant change in electrical properties [4]. Both VO_x and a-Si microbolometers are affected [5]. As a result, the microbolometer IRFPA will produce a persistent afterimage when the source is removed [6]. This issue can be observed when the microbolometer is exposed to a high temperature source such as fire, explosion, or sun, and it is sometimes referred to as the "sunburn" effect [7]. Although a shutter-based nonuniformity correction can mitigate this effect, a latent image reappears rapidly after shutter operation and persists with a very long decay time.

Thus, there is a need for an uncooled infrared detector that can withstand high-temperature exposure. This requirement will be all the more significant as the pixel pitch is reduced. Indeed, the design of a smaller pixel involves a thermal insulation enhancement that exceeds the reduction of the optical sensitive area in order to maintain the same NETD as the pixel pitch is reduced.

To address this issue, we suggest a pixel architecture whose arrangement calls for the replacement of the current thermistor by a high-frequency mechanical nanoresonator designed to be ultrasensitive to IR radiation. The high-frequency stability of these mechanical resonators should allow us to reach the fundamental phonon noise and avoid large thermal insulation while keeping a high scene resolution. Within this approach, the sunburn effect should no longer be a limiting element for downscaling the pixel size.

Similar approaches based on silicon [8–13], quartz [14–16], AlN [17,18], or GaN [19] resonators have already been suggested. More recently, whispering-gallery-mode optical resonators have also been proposed [20,21]. These different approaches have barely reached a pixel pitch below 100 μm and are, therefore, not suitable for uncooled infrared imaging. It still remains a challenge to build a resonator with 12-μm pitch and a fully integrated readout inherent of a compact imager (usually done through a postprocess of imager on the CMOS readout electronics circuit).

Recently, nanoelectromechanical systems (NEMSs) have shown great promise for technological applications, in particular, for integrated frequency clocks [22], logic switches [23], mixer filters [24], ultrasensitive force detectors [25], and mass sensors [26]. To increase the capture cross section without losing their extreme sensitivity, NEMS sensor arrays have been advantageously used, even sometimes cointegrated with CMOS electronics [27,28]. In the framework of very large-scale integration, implementation of billions of IR highly sensitive nanoresonators in a dense array is at hand [29]. We present here a 12-μm-pitch NEMS resonator that we fully characterize in a closed-loop scheme through a phase-locked loop (PLL). This work intends to tackle the three main points to let resonating IR sensors emerge: (i) a low-temperature fabrication process to be fully compatible with the cointegration approach on the CMOS readout circuit, (ii) a low-noise transduction scheme based on capacitive detection and electrostatic actuation for avoiding the self-heating phenomenon and decreasing 1/f noise, and (iii) a low-noise electronics circuit for an efficient readout of tiny capacitance variation.

II. DESIGN AND FABRICATION OF NEMS ARRAYS

Contrary to NEMS approaches that are usually used to get stable nanoresonators, we choose a low-temperature fabrication process, which is inherited from classical bolometers (i.e., deposition process $<300\,^{\circ}$C and above-IC compatible). Two silicon nitride layers of 10 nm encapsulate a titanium nitride layer which acts as an electrode as well as an absorber. SiN features a high Young's modulus and low thermal conductivity, which makes it a suitable material for long and narrow insulating rods. A 150-nm layer of amorphous silicon is then deposited to have a stiff enough resonator. Unlike the resistive bolometer, no electrical connection is needed here between TiN and a-Si, thereby simplifying the process. Several designs are defined depending on the length of the torsional rods and the thickness of a-Si on the insulation rods. A $\lambda/4$ cavity is formed between the reflecting electrodes and the paddle by removing the polymer using plasma chemical releasing (the resonant Fabry-Pérot cavity is centered at 8 μm). The thickness of the TiN is chosen to match the impedance of vacuum (376.7 Ω) and minimize the incident wave reflection leading to 50% absorption efficiency. In our $\lambda/4$ configuration, this absorption of the bolometer is improved and tends toward 1 in the (8–14)-μm atmospheric window. To drive and read our resonant electromechanical sensor, we split the reflecting electrode into two electrodes for electrostatic actuation and capacitive sensing, respectively. The TiN incorporated into the paddle is polarized in order to raise a capacitive sensing signal. The electrostatic torque applied enables the torsion of suspended rods. The detailed fabrication process is provided in Appendix A of the Supplemental Material [30].

Figure 1 shows some structures magnified by a scanning electronic microscope (SEM). The nominal single pixel is presented in Fig. 1(b), and its integration in an array is presented in Fig. 1(a). One can observe the actuation and sensing electrodes beneath the suspended paddle as well as the strip lines going into the

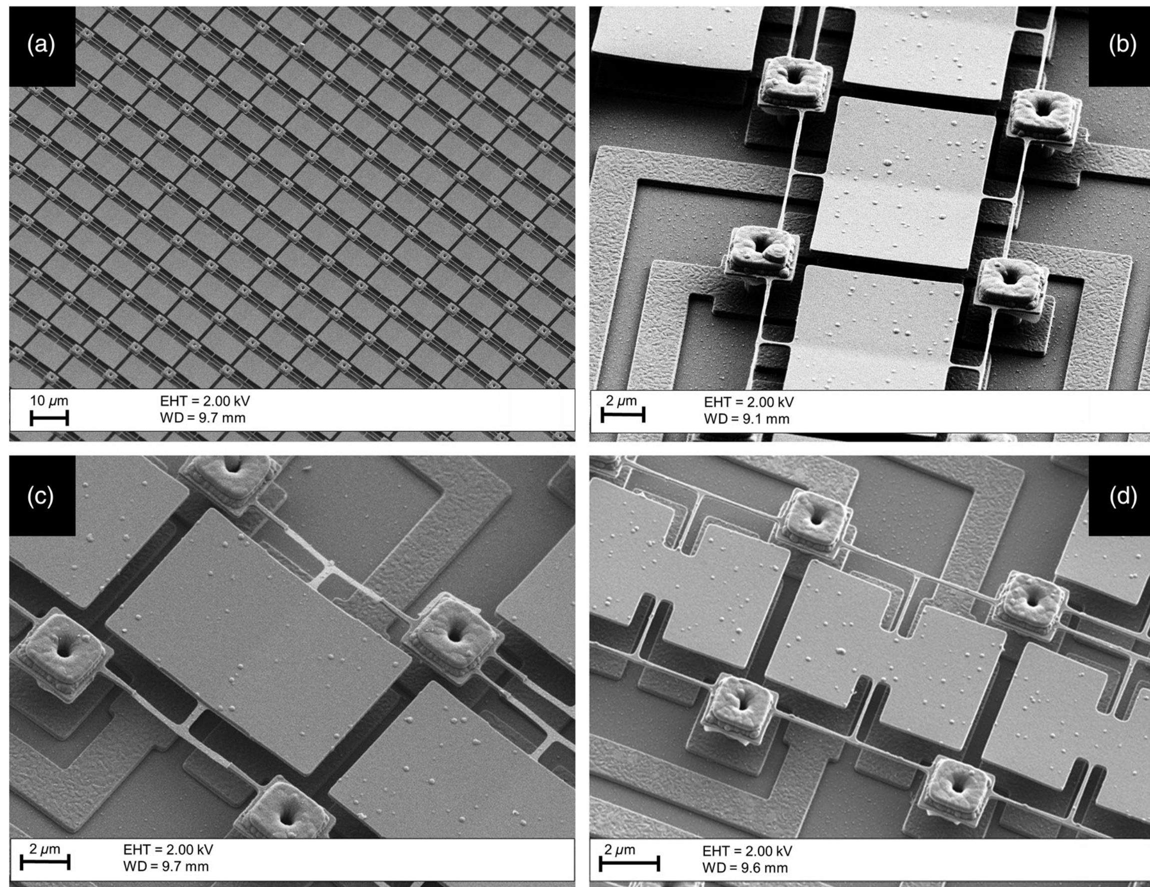

FIG. 1. SEM images of the bolometer. (a) SEM image of the typical matrix of microelectromechanical pixels. (b) SEM picture of a typical H-shaped pixel; nanorod length = 1.5 μm, width = 250 nm, and thickness = 180 nm (insulation arm length = 8.6 μm). (c) SEM picture of another H-shaped pixel with a thinner nanorod to enhance the thermal insulation; rod thickness = 30 nm. (d) SEM image of a butterfly-shaped pixel with longer rods.

anchors for the electrical polarization. Two other designs are shown in Figs. 1(c) and 1(d). Table I summarizes some key parameters of the fabricated sensors. In particular, a comparison with a classical bolometer is displayed. Our temperature sensitivity is 3 orders of magnitude below the resistive bolometer. Nevertheless, the noise frequency of our oscillating thermal sensor is usually much lower, which offsets this low thermal response [10].

III. SENSOR OPERATION

The microsystem is excited at its first torsion mode using an actuation electrode placed under the plate. A

TABLE I. Key parameters of our device compared with an advanced resistive bolometer and MEMS bolometer: temperature sensitivity corresponds to $1/T \times \partial f/\partial T$ for the resonant thermal sensor and $1/T \times \partial R/\partial T$ for the resistive sensor.

	This work [Fig. 1(b)]	Bolometer [1]	Resonant MEMS [10]
Pitch (μm)	12	12	5
Thermal conductance G (W/K)	5×10^{-8}	5×10^{-9}	1.5×10^{-8}
Thermal capacity C (J/K)	26×10^{-12}	80×10^{-12}	3×10^{-12}
Thermal constant τ_{th} (ms)	0.5	16	0.2
Temperature sensitivity (/°C)	0.01%	3.6%	0.0092%
Stiffness κ (N m)	1.8×10^{-11}	Not applicable	6.8×10^{-13}
Inertia moment J (kg m^2)	3.9×10^{-25}	Not applicable	1.5×10^{-27}
Quality factor Q	1800	Not applicable	1555

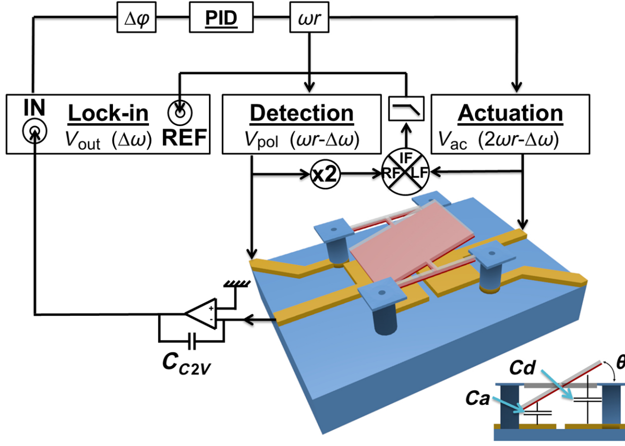

FIG. 2. Schematic of the MEMS and NEMS resonator and readout scheme. Capacitive MEMS and NEMS resonator embedded in a downmixed phase-locked loop. The electrostatic actuation is done at $2\omega_r + \Delta\omega$, and the plate is polarized at $\omega_r + \Delta\omega$ to get a downmixed signal at $\Delta\omega$ that feeds the lock-in amplifier input. A transimpedance circuit is specifically designed for measuring tiny capacitance variations due to the torsional vibration of the plate.

closed loop (phase-locked loop) is used to maintain the oscillations at its resonance frequency, as shown in Fig. 2. An incident infrared electromagnetic wave is absorbed by the layer deposited on top of the plate and causes its heating by the Joule effect. Thereby, the internal temperature rise induces a variation of the torsional resonance frequency. This frequency shift is mainly due to changes in the Young's modulus and internal stresses. The frequency is then measured through a capacitive signal between the detection electrode and the oscillating plate. A dedicated readout electronics board based on a transimpedance circuit (see Fig. 2) is carefully developed for measuring the tiny capacitance variation (approximately 30 aF) compared to both the capacitance at rest (approximately 0.18 fF) and the parasitic capacitance (approximately 1 pF). The pixels are directly connected by wire bonding on the readout board to minimize the parasitic capacitance. A HF2 lock-in instrument from Zurich Instruments is used to perform synchronous detection. A complete description of our experimental setup is provided in Appendix D of the Supplemental Material [30]. Moreover, a downmixing detection scheme is chosen to get rid of the feedthrough [31].

For the sake of clarity, below we provide the main electromechanical equations required for understanding the experimental characterizations. We focus only on the first torsional mode. The electrical torque induced by the excitation electrode will actuate the plate with an angle θ (see Fig. 2) according to the dynamic equation

$$J\ddot{\theta} + b\dot{\theta} + \kappa\theta = T_e,$$
$$T_e = \frac{1}{2}\frac{dC_a}{d\theta}(V_{ac} - V_{pol})^2 + \frac{1}{2}\frac{dC_d}{d\theta}V_{pol}{}^2, \qquad (1)$$

where C_a and C_d are the actuation and detection capacitances, respectively (see Fig. 2), V_{pol} is the polarization voltage of the plate, and V_{ac} is the actuation voltage. Considering the transimpedance circuit, the output signal reads

$$V_{out} = \frac{V_{pol}}{2}\frac{C_0}{2C_{C2V}}\frac{\theta_{max}}{\theta}\ln\left[\left(1-\frac{\theta}{\theta_{max}}\right)\left(1+\frac{\theta}{\theta_{max}}\right)\right], \qquad (2)$$

with C_0 the static detection capacitance and θ_{max} the maximum geometric angle (corresponding to the paddle sticking on the electrode, $-20°$ here). For a complete presentation of mathematical computations, please refer to Appendix B of the Supplemental Material [30].

IV. RESULTS

A. Electromechanical performance

Let us focus on the basic electromechanical experiments. We perform a frequency sweep of the actuation signal to find the resonance frequency and determine the quality factor from a Lorentzian fit in the complex plane. The typical results obtained with the device outlined in Table I are shown in Figs. 3(a) and 3(b). At first sight, the experimental output voltages are in good agreement with those computed from our electromechanical model. The quality factor Q extracted from this measurement at $P = 5\times10^{-5}$ mbar is equal to 1800; the quality factors are between 900 and 3000 depending on the pixel designs. Remarkably, we are able to routinely measure 30-aF capacitance variation at resonance for a static capacitance of 0.18 fF and a signal-to-background ratio of 22 dB; the smallest capacitance variation measured is 2.6 aF. Electromechanical responses with frequency and V_{ac} (at $V_{pol} = 10$ V) are plotted in Fig. 3(c). As expected, the output voltage at resonance is clearly proportional to V_{ac}^2. Similarly, the responses with frequency and V_{pol} (at $V_{ac} = 6.5$ V) are plotted in Fig. 3(d). The output voltage at resonance is logically proportional to V_{pol}.

Beyond a critical angle θ_c [32], the uniqueness of the solution to Eq. (1) is not preserved, and the linear behavior of our device disappears. $\theta_c = 13°$ sets the onset of nonlinearity of our typical device outlined in Table I. Hardening, softening, or even the compensation of both effects (see, for example, Refs. [33,34]) are observed on these devices. In particular, the compensation of nonlinearities is found for stiff arms, leading to a linear operation range up to 13° and output voltages up to 320 μV at 10-V polarization voltage.

B. Electro-optical performance

Let us now focus our study on the thermal response R_f (/W) of one pixel. R_f is defined as the ratio of the relative frequency shift f/f_0 to the incident power P_{inc}:

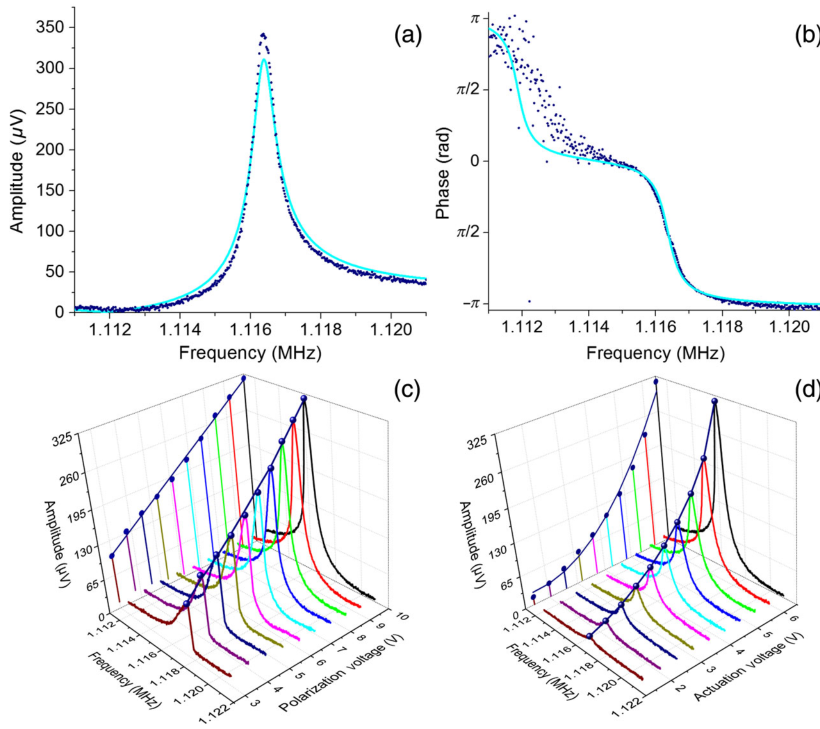

FIG. 3. Typical electromechanical responses. (a) Amplitude of a typical frequency response for a device with a mechanical stiffness close to $\kappa \sim 2.0 \times 10^{-11}$ N m (dots). (b) Phase of a typical frequency response of the same device. We extract a quality factor of 1800 from a Lorentzian fit (light blue line), considering first and last quarters of the spectrum as background (the slight discrepancy observed at resonance is due to the presence of nonlinear terms, which are not included in the fit). (c) Electromechanical response according to frequency and actuation voltage V_{ac} ($V_{\mathrm{pol}} = 10$ V). As expected, the voltage at resonance is proportional to V_{ac}^2. (d) The amplitude according to the frequency and polarization of the plate V_{pol} ($V_{\mathrm{ac}} = 6.5$ V). As expected, the voltage at resonance is proportional to V_{pol}.

$$\Delta f = \frac{\alpha_T f_0 \beta \eta}{G|1 + j2\pi\nu\tau_{\mathrm{th}}|} P_{\mathrm{inc}} = f_0 R_f P_{\mathrm{inc}}. \quad (3)$$

$\tau_{\mathrm{th}} = C/G$ is the thermal time constant of the sensor, $C = (\partial U/\partial T)_V$ is the thermal capacitance at constant volume, G is the thermal conductance, α_T is the temperature coefficient of frequency (typically, -60 ppm/°C for silicon), β is the pixel fill factor, η is the bolometer absorption, f_0 is the resonance frequency, and ν is the frame rate of the electronic readout. This expression is used later at the end of the paper to verify the coherence of the experimental values.

The main features that we introduce above are experimentally measured through our readout scheme shown in Fig. 2. All measurements reported here are done with the same device introduced in Table I. The typical results and the best results are systematically presented. We embed our system in a downmixed PLL to track the resonance frequency in real time. This closed loop allows us to measure instantaneously the IR responsivity and the frequency noise. The electronics board with pixels under test is placed into a homemade vacuum chamber that is illuminated by a blackbody source. The noise-equivalent power (NEP) of our sensor can be then computed from these measurements. We also perform temperature coefficient of frequency (TCF) measurements to compute the theoretical responsivity from Eq. (3). The measurements are performed with a coupled Peltier Pt sensor controlled by a proportional integral derivative controller that provides the chamber temperature (down to 0.1 °C accuracy). Some of the results for several devices are displayed in Appendix D of the Supplemental Material [30]. A typical TCF of $\alpha_T = -70$ ppm/°C is extracted from this experiment, and it is consistent with the values commonly reported in the literature.

A commercial blackbody RCN 1200 from HGH Infrared Systems (set at 1200 °C) is placed in front of the vacuum chamber. An (8–12)-μm filter is positioned between our chamber and the source to control the incident power. The optical bench is aligned using a visible laser. The overall experimental setup is detailed in Appendix D of the Supplemental Material [30].

The entire optics is calibrated using a Fourier-transform infrared instrument. In particular, the spectral response of the filter according to the spectral luminance of a perfect blackbody at 1200 °C is measured to determine the incident optical power through the equation below (see Appendix D of the Supplemental Material [30] for more details),

$$P_{\mathrm{inc}} = S_{\mathrm{bolo}} \pi \sin^2(\theta_m) \int_0^\infty L_\lambda^0 T_{\mathrm{opt}} d\lambda, \quad (4)$$

where S_{bolo} is the surface of our device, L_λ^0 is the spectral luminance of a perfect blackbody, and T_{opt} is the optical transmittance. Here, our resonant bolometer is 8.6 cm away from the blackbody emissive surface, which has a diameter aperture of $\Phi_{\mathrm{BB}} = 25$ mm. The frequency response of our pixel (given in Table I) to IR incident pulses (26-nW peak) is presented in Fig. 4. The frequency drift observed when hiding the IR source is attributed to the chip heating induced by the close 1200 °C source. A typical experimental thermal response $R_f = 720\,\mathrm{W}^{-1}$ is extracted from this measurement. Assuming a fill factor of $\beta = 0.8$, an efficiency $\eta = 0.8$ in the (8–12)-μm window, and

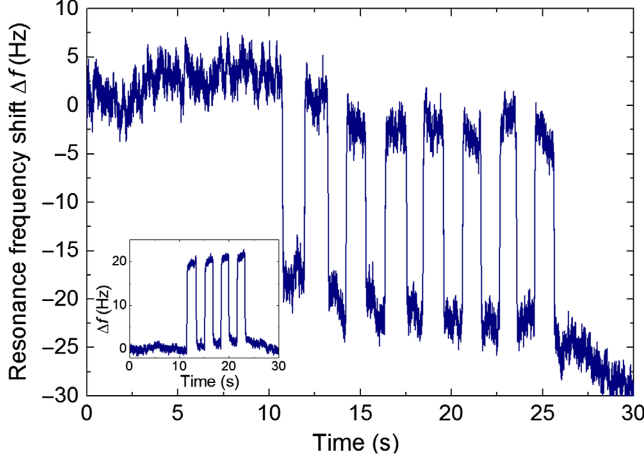

FIG. 4. Frequency response. IR illumination corresponds to 26-nW incident power. This power provokes 21-Hz frequency shift (i.e., $R_f = 720\,\mathrm{W}^{-1}$). The acquisition is performed in the closed-loop scheme for an integration time of 1 ms. Inset: Similar measurement done with 17-nW incident power on one of the best devices (20-Hz frequency shift is observed in this case).

considering the measured TCF $\alpha_T = -70$ ppm/°C, the theoretical thermal response $R_f = 900\,\mathrm{W}^{-1}$ is expected, which is very close from the observed sensitivities. The discrepancy may be due to the uncertainty of the real bolometer temperature when performing the TCF measurements. Thermal responses up to $R_f = 1050\,\mathrm{W}^{-1}$ are obtained with the best devices (see inset in Fig. 4).

C. Frequency noise

We now move on the detection limit of the IR sensor. The performance of infrared detectors is usually evaluated through the NEP or the noise-equivalent temperature difference (NETD). The NEP is defined as the incident power on the sensor surface to obtain a SNR = 1,

$$\mathrm{NEP} = \frac{\delta f / f_0}{R_f(\nu = 0)}, \tag{5}$$

where δf are the rms frequency fluctuations for a given noise bandwidth.

Most of the imager's electronics relies on the so-called column readout that is the current approach with CMOS circuits. In principle, such "column" or "rolling-shutter" readout schemes can be implemented for our resonator array. Before designing and fabricating such a dedicated readout circuit (ROIC), the electromechanical features of our resonators have to be properly measured. The characterizations are achieved considering the measurement conditions used in a typical ROIC: the integration time of a single pixel is divided by the number of pixels inside the column (typically, for a 60-Hz frame rate, the pixel integration bandwidth is 7 kHz for 190 pixels per column) [35]. With this readout scheme, a lag effect may appear leading to image distortion when the scene moves faster than the frame rate. On the contrary, single-pixel readout enables us to cancel this effect. The integration time can be increased to the full frame rate, i.e., 50 Hz, thereby increasing the SNR. However, the whole circuit footprint has to correspond to the pixel pitch, making it more complex to implement. As the frequency readout scheme does not suffer from a self-heating issue, it is possible to use a long integration time without material degradation even for small pitch below 12 μm. That is why the NEP of our sensor is estimated for the two noise bandwidths of 7 kHz and 50 Hz.

The overall NEP is defined as the quadratic sum of uncorrelated noises $\mathrm{NEP} = \sqrt{\sum_i \mathrm{NEP}_i^2}$, where NEP_i is the power density of the noise i, namely, the phonon noise, thermomechanical noise, and electronics noise. The resulting NETD that defines the sensor resolution on the scene can be immediately deduced from the overall NEP,

$$\mathrm{NETD} = \frac{4F^2}{\pi A_p \Phi_{\lambda_1\to\lambda_2} \left(\frac{\Delta L}{\Delta T}\right)_{300\ \mathrm{K}_{\lambda_1\to\lambda_2}}} \mathrm{NEP}, \tag{6}$$

where F is the optical aperture (usually $F = 1$), A_p is the pixel surface, and Φ and $\Delta L/\Delta T$ are the optical transmission and the luminance variation with the scene temperature around 300 K, both evaluated in the $[\lambda_1; \lambda_2]$ range. In the (8–14)-μm range, Φ is usually close to 1, and $\Delta L/\Delta T$ is evaluated as 0.84 W/m^2/sr/K [36].

The fundamental source of noise (for a thermal conductance higher than the radiation conductance; see Appendix C of the Supplemental Material [30]) should be the phonon noise resulting from the random exchange of heat between the sensor and the thermal bath through the mechanical supports. For a bandwidth higher than $1/4\tau_{\mathrm{th}}$ (which is commonly the case for IR imagers), the phonon NEP reads

$$\mathrm{NEP}_{\mathrm{phonon}} = \frac{G}{\beta\eta}\sqrt{\frac{k_B T^2}{C}}. \tag{7}$$

All mechanical sensors struggle with the fundamental thermomechanical noise due to the coupling with the ambient thermal bath. The power spectral density of the thermochemical noise is $S_\theta(\omega) = (2k_B T/Q)\kappa\omega_0^3/[({\omega_0}^2 - \omega^2)^2 + (\omega\omega_0/Q)^2]$, where k_B is the Boltzmann constant, Q is the quality factor of the resonator, κ is the mechanical stiffness, ω_0 is the angular resonance frequency, and T is the temperature of the device. We are interested in the frequency random fluctuation whose frequency-noise power spectral density can be easily deduced from $S_\theta(\omega)$ through the expression [37,38] $S_\omega(\omega) = (\omega_0/2Q)^2 S_\theta/\theta_c^2$. Finally, the thermomechanical NEP is expressed using the thermal response R_f,

TABLE II. NEP computation for the nominal design with our homemade electronics and downmixing readout scheme: $R_f = 720\,\mathrm{W}^{-1}$, $\beta\eta = 0.64$, $\theta_C = 13°$, $V_n = 10\ \mathrm{nV}/\sqrt{\mathrm{Hz}}$, and $V_{\mathrm{out}} = 320\ \mu\mathrm{V}$ (see Appendix C of the Supplemental Material [30] for the complete computation of the thermomechanical and electronics noises).

	$\mathrm{NEP}_{\mathrm{phonon}}$ (pW)	$\mathrm{NEP}_{\mathrm{thermo}}$ (pW)	$\mathrm{NEP}_{\mathrm{elec}}$ (pW)	NEP (pW)	NETD (K)
1-Hz bandwidth	0.8	0.85	12	12	0.13
50-Hz bandwidth	5.5	6	85	85	0.9
7-kHz bandwidth	17	25.5	1000	1000	10.5

$$\mathrm{NEP}_{\mathrm{thermo}} = \frac{1}{R_f}\frac{1}{2Q}\frac{\sqrt{\frac{1}{2\pi}\int_{\omega_0-(\Delta\omega/2)}^{\omega_0+(\Delta\omega/2)} S_\theta(\omega)d\omega}}{\theta_c} \leftrightarrow \frac{1}{R_f}\frac{1}{2Q}\frac{\sqrt{\langle\theta_n^2\rangle}}{\theta_c}, \tag{8}$$

where $\Delta\omega$ is the noise bandwidth. The electronics noise arising from readout circuit may be not negligible compared to the signal to be detected (a comprehensive model is presented in Appendix D of the Supplemental Material [30]). The expected electronics NEP is similar to Eq. (8):

$$\mathrm{NEP}_{\mathrm{elec}} = \frac{1}{R_f}\frac{1}{2Q}\frac{\sqrt{\langle V_n^2\rangle}}{V_{\mathrm{out}}}. \tag{9}$$

Through Eqs. (5)–(9), the theoretical NEPs due to the different contributions are estimated for our nominal design [Table I and Fig. 1(b)] and are summarized in Table II. We notice that our electronics noise will be theoretically the main noise source. It can be minimized by a factor of 2 (direct detection instead of downmixing; see Appendix D of the Supplemental Material [30]) using a dedicated ROIC with lower parasitic capacitance (a few femtofarads instead of 1 pF). Furthermore, a pixelwise readout (50-Hz bandwidth) will improve the NETD down to 450 mK. For a 1-s integration time, the NETD reaches 65 mK, which is close to current bolometer performance at 12-μm pixel pitch with a 10 times shorter thermal time constant.

The experimental NEP is deduced from the normalized frequency stability $\delta\omega/\omega_0$ [Eq. (5)]. To this end, we measure the Allan deviation [39] σ_A of the output signal versus integration time τ. The Allan deviation measurements of the three designs (see Fig. 1) are performed both in open-loop and closed-loop (PLL) configurations. In closed loop, the instantaneous frequency is estimated and kept constant. In open loop, the resonator is driven at fixed frequency close to resonance, and the phase data $\Delta\varphi$ are recorded. In this case, σ_A is deduced from these data with the simple expression $\delta f = \delta\varphi/2Q$ [38].

For the sake of clarity, only the Allan deviations measured in closed loop are presented in Fig. 5 for the typical and best devices (see inset). Open-loop measurements lead to very similar data. σ_A exhibits a $\tau^{1/2}$ slope between 70 μs and 10 ms, showing that white noise is the main contribution in this interval. According to our previous calculations, its origin is mainly attributed to the readout electronics. A plateau, which corresponds to a 1/f-frequency noise, appears at higher integration time. This long-term noise is well above the noise floor normally set by the thermomechanical and phonon noises (close to 1×10^{-8} for the two noise sources). Supplemental experiments are conducted to analyze the source of the 1/f noise (please refer to Appendix D of the Supplemental Material [30]). We demonstrate that the plateau is independent of the signal-to-noise ratio. We believe that this noise is not due to amplitude random fluctuations but may be inherent in pure frequency fluctuation. Similar noise signature [reported as an anomalous phase noise (APN)] has been recently reported for flexural nanoresonators having similar mode volume [40]. More investigations are necessary to confirm this noise source. In the meantime, the stability limit of our

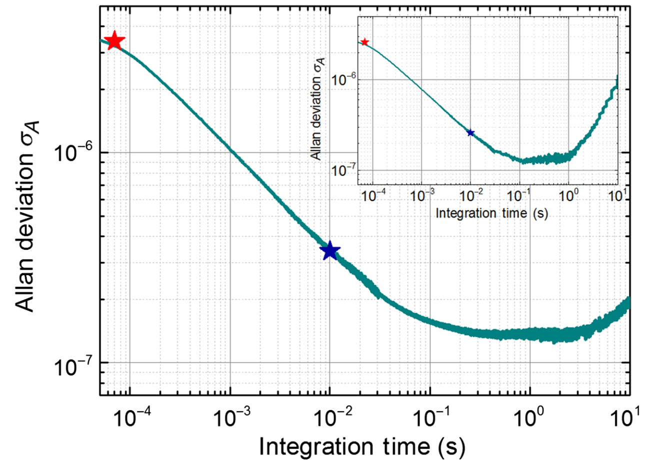

FIG. 5. Allan deviation measurement ($V_{\mathrm{pol}} = 10$ V and $V_{\mathrm{ac}} = 1.75$ V). The red star is the frequency deviation at 7-kHz integration bandwidth ($\sigma_A = 3.5\times10^{-6}$), and the blue star is the frequency deviation at 50-Hz integration bandwidth $\sigma_A = 3\times10^{-7}$; 50 Hz and 7 kHz correspond to 20 ms and 70 μs, respectively [35]. The minimum frequency noise ($\sigma_A = 1.5\times10^{-7}$) is reached for longer integration times between 50 and 200 ms. Inset: Similar measurement done with the best device [$\sigma_A(70\ \mu\mathrm{s}) = 2.5\times10^{-6}$ and $\sigma_A(20\ \mathrm{ms}) = 2\times10^{-7}$].

TABLE III. Comparison of the key features of three designs. The thermal conductance of the second device is improved compared to the first design by removing the amorphous silicon on the insulation rods. It greatly improves the thermal isolation but decreases the mechanical stiffness and deteriorates the linear dynamic range. In the third design, the torsional rod length is increased from 1.5 to 3.8 μm, which improves the thermal isolation but also greatly deteriorates the linear dynamic range.

Pixel design	G_{th} (nW/K)	θ_c	Q	R_f (/W$_{inc}$)	NEP (nW) (100 ms)	NEP (nW) (20 ms)	NEP (nW) (0.7 ms)
Figure 1(b) (nominal design; typical results)	50	13°	1800	720	0.21	0.41	4.9
Figure 1(b) (nominal design; best results)	50	12°	2400	1050	0.14	0.19	2.4
Figure 1(c) (thinner rod)	18	0.7°	900	3555	1.3	3	35
Figure 1(d) (butterfly design)	31	2.5°	2400	1011	0.47	1.1	12

torsional devices is set by this anomalous phase noise and can be considered as the fundamental limit for our resonant sensors.

V. DISCUSSION

From Eqs. (5) and (6), the NEP and NETD are extracted for the three designs, in particular, for a typical device ($R_f = 720\,\mathrm{W}^{-1}$) and the best device ($R_f = 1050\,\mathrm{W}^{-1}$). Table III provides an overview of the main features. From Table III, it seems obvious that the thermal response R_f will be large, especially as the thermal insulation $1/G$ is high. In addition, the signal-to-noise ratio will be large, especially as the torque angle is high, i.e., a mechanical stiffness as low as possible. Intuitively, these requirements are met with long and thin rods made of material with low thermal conductivity.

However, the onset of nonlinearity may be more quickly reached with soft springs due to the electrostatic nonlinear effect (reducing significantly the critical angle value θ_C). A trade-off between the thermal insulation requirement and large critical angle has to be found. The length and shape of the arms are, in particular, optimized to find the best compromise. Our nominal design meets this compromise with rigid springs ($\kappa \sim 2 \times 10^{-11}$ N m) and high torsional resonance frequency (around 1 MHz).

Whatever the tested designs (the isolation rods' length, thickness, and stress), we do not observe a major difference in terms of TCF ranging from −35 to −100 ppm/°C (please refer to Appendix D of the Supplemental Material [30]). Unfortunately, the highest TCF occurs with soft devices, which are not suitable for IR sensing, as we explain above. Remarkably, a compensation of hardening and softening nonlinear terms [33] are observed with the nominal geometry leading to a critical angle up to 13° (50% of θ_{max}) keeping the thermal conductance as low as 5×10^{-8} W/K. In this case, the mechanical dynamic range, which is the ratio between the onset of nonlinearity and the thermomechanical noise, is around 113 dB.

Experimental NEPs at 50 Hz and 7 kHz of the best device are close to the values obtained through Eqs. (5)–(9) considering $R_f = 1050\,\mathrm{W}^{-1}$ and the experimental value of the electronics noise $40\,\mathrm{nV}/\sqrt{\mathrm{Hz}}$. A sensitivity to (8–12)-μm radiation below 27 nV/$\sqrt{\mathrm{Hz}}$ can be reached leading to a NETD of 2 K at 50 Hz (NETD = 1.5 K at 100 ms) with a submillisecond response time. At a long integration time, the fundamental limit normally set by the phonon noise is not reached due to the anomalous phase noise. The noise analysis informs us that the readout electronics per column at 7 kHz currently used for resistive bolometers is not suitable for our approach.

Nevertheless, a cointegration of the electronics at pixel level will reduce the parasitic capacitance down to a few femtofarads corresponding to the input capacitance of a transistor and will decrease the electrical noise down to a theoretical level of 10 nV/$\sqrt{\mathrm{Hz}}$, which is 4 times lower than our experimental noise. Moreover, this approach makes the heterodyne detection scheme unnecessary and improves the signal by a factor of 2. The contribution of electronics noise to σ_A and the NEP will be accordingly decreased by a factor of 8 [see Eq. (9)]. In these conditions, a noise bandwidth larger than the frame rate bandwidth will not deteriorate the resonator noise. For instance, an Allan deviation $\sigma_A = 1.75 \times 10^{-7}$ is expected considering both the plateau contribution (APN) and the electronic noise for a 700-Hz noise bandwidth. This configuration allows us to read 700/50 = 14 pixels during the frame rate, which allows a larger area for the cointegrated readout.

To better assess the performance of our component, the main features are compared with the best results reported in the literature. A comparison criterion is the figure of merit FOM = NETD × τ_{th} × A_p, where the τ_{th} (ms) and A_p (μm^2) are the thermal constant and the pixel pitch, respectively, and the NETD is expressed in millikelvins. Indeed, since the NETD and τ_{th} are usually kept constant (<50 mK, 10 ms) when decreasing the pixel pitch, the FOM is introduced in order to evaluate at a glance the quality of the microbolometer technology [41]. Basically, this FOM removes the dependence of the sensor performance with the thermal conductance and surface absorption (i.e., independent of geometrical considerations). The performance reported in this paper stands out more clearly by considering the FOM according to the pitch for several

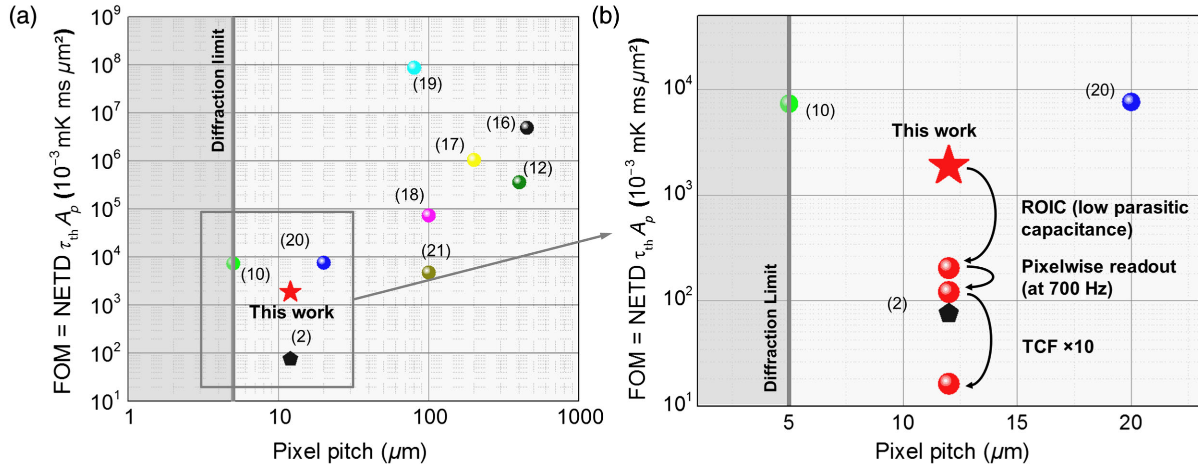

FIG. 6. The FOM versus pitch. Comparison with work recently reported in the literature. Symbols: spheres correspond to devices based on frequency detection; pentagons are resistive detection. (a) The FOM tends to drop, demonstrating a continuous improvement of resonant MEMS bolometers. The FOM of our device is 1 order of magnitude higher than the values exhibited by the resistive sensor [1]. (b) Extrapolated FOM of our thermal sensor according to cumulative assumptions: (i) integration of our sensor on a CMOS circuit, (ii) pixelwise readout rate, and (iii) improvement of the thermal response through TCF enhancement (×10).

works recently reported in the literature (Fig. 6). The FOMs of our best device are extracted from Allan deviation measurements: $\mathrm{FOM}(50\,\mathrm{Hz}) = 144\times10^3\,\mathrm{mK\,ms}\,\mu\mathrm{m}^2$ and $\mathrm{FOM}(7\ \mathrm{kHz}) = 1810\times10^3\ \mathrm{mK\,ms}\,\mu\mathrm{m}^2$.

VI. PERSPECTIVES

Because of the strong parasitic capacitance related to our homemade electronics and the low-temperature sensitivity, our resonant nanosensors are still far away from resistive bolometer performance. We believe that the use of a ROIC with self-oscillating circuits for a few tens of pixels will easily decrease the NEP. In this case, a 700-Hz integration bandwidth will be used, and the noise will drop to the fundamental limit set by the anomalous phase noise of the NEMS. Moreover, the readout electronics input impedance will be close to a few femtofarads, which will increase the useful signal. The NEP will be lower than 165 pW with a thermal constant of 0.5 ms, which is 20 times faster than the current bolometer. The FOM will be close to 10^5 (12-μm pixel). The optical readout can also be particularly suitable for multiplexing and high-efficiency transduction mechanism.

Even if very low noise can be reached with such an approach, the thermal response R_f is not high enough to surpass the resistive bolometers. The evident solution may consist of using a stiffer material with lower thermal conductivity to decrease the thermal conductance down to 5×10^{-9} W/K preserving the large dynamic range (large critical angle θ_c). The porous material can be improved for thermal insulation, keeping the same stiffness. A 2D phononic crystal should also be studied, but we emphasize that an excessive thermal insulation can lead to significant change in the thermometer properties because of the sunburn effect, especially when shrinking the device size. We rather focus our discussion on increasing the TCF of our devices. Some interesting work has already shown a TCF up to 1000 ppm/°C, thereby improving the TCF by a factor of 20 [9,11]. In particular, the first-order phase transition of diverse materials has been used to obtain a Young's modulus that is highly sensitive to the temperature [42,43]. These works initiate a promising way to reach a high TCF. Improving significantly the temperature sensitivity of our devices will likely stimulate these research axes.

With both an improvement of the frequency response of a factor of 10 and a pixelwise readout, the NEP will be lower than 20 pW (NETD $<$ 180 mK) with $\tau_{th} = 0.5$ ms, and the FOM will drop to 10^4. This projection tends to demonstrate that uncooled IR sensors based on a nanomechanical resonator will generate interest for small pitch below 12 μm.

VII. CONCLUSION

In conclusion, we demonstrate the great potential of a high-frequency resonant sensor fabricated with a low-temperature process dedicated to uncooled infrared imaging. A complete electrical transduction is developed to drive and read the useful signal according to calibrated temperature variations. We are able to extract all key parameters to compare our approach with previous resonant thermal sensors and resistive bolometers. The low-temperature process we use here gives the perspective of above-IC integration and, therefore, dense low-cost imagers. A high dynamic range corresponding to a torque angle up to 13°, i.e., 50% of the gap (113 dB), is demonstrated. That enables us to enhance the output electromechanical signal. A NEP of 190 pW is measured with our system at 50-Hz integration time. With a

cointegrated electronics, which reads 14 pixels in a 700-Hz bandwidth through an above-IC self-oscillating loop, the NEP should drop to 165 pW, close to the anomalous phase noise of the resonant sensor that definitively sets the fundamental limit. As the self-heating is canceled by using the capacitive transduction, this longer integration time will not lead to excessive heating of the membrane.

However, to surpass the bolometers below 12-μm pitch, the temperature sensitivity has to be increased at least by a factor of 10. To this end, work based on first-order phase-transition material should allow us to increase the frequency response through a large improvement of the TCF. Otherwise, an improvement of the thermal insulation by a factor of 10 is also conceivable and may lead to a NEP close to 15 pW. Within these two approaches, a NEP around 1.5 pW, or a NETD of 17 mK, and a FOM between 1 and 10 can be expected This trend will certainly renew interest in resonant uncooled IR sensors for current and future pitch generation.

ACKNOWLEDGMENTS

The authors acknowledge financial support from the LETI Carnot Institute MOTION project. They also thank P. Imperinetti, M. Sansa, and G. Jourdan for their helpful support with the component fabrication and characterizations.

[1] T. Endoh *et al.*, Uncooled infrared detector with 12 μm pixel pitch video graphics array, Proc. SPIE Int. Soc. Opt. Eng. **8704**, 87041G (2013).

[2] FLIR Boson®, FLIR Systems, http://www.flir.com/cores/boson/.

[3] TWV640 Thermal Camera Core, BAE Systems International, http://www.baesystems.com/en/product/twv640-thermal-camera-core.

[4] Y. Jo, I.-W. Kwon, D. S. Kim, H. Bin Shim, and H. C. Lee, A self-protecting uncooled microbolometer structure for uncooled microbolometer, Proc. SPIE Int. Soc. Opt. Eng. **8012**, 80121O (2011).

[5] D. A. Dorn, O. Herrera, C. Tesdahl, E. Shumard, and Y.-W. Wang, Impacts and mitigation strategies of Sun exposure on uncooled microbolometer image sensors, Proc. SPIE Int. Soc. Opt. Eng. **8012**, 80123Z (2011).

[6] J. L. Tissot *et al.*, High performance uncooled amorphous silicon VGA IRFPA with 17 μm pixel-pitch, Proc. SPIE Int. Soc. Opt. Eng. **7660**, 76600T (2010).

[7] A. Fraenkel *et al.*, VO*x*-based uncooled micrbolometric detectors: Recent developments at SCD, Proc. SPIE Int. Soc. Opt. Eng. **6206**, 62061C (2006).

[8] J. E. Ralph, R. C. King, J. E. Curran, and J. S. Page, Miniature quartz resonator thermal detector, in *Proceedings of the IEEE Ultrasonics Symposium, San Francisco, CA, USA* (1985), p. 362, DOI: 10.1109/ULTSYM.1985.198533.

[9] C. Cabuz, S. Shoji, K. Fukatsu, E. Cabuz, K. Minami, and M. Esashi, Fabrication and packaging of a resonant infrared sensor integrated in silicon, Sens. Actuators A **43**, 92 (1994).

[10] X. C. Zhang, E. B. Myers, J. E. Sader, and M. L. Roukes, Nanomechanical torsional resonators for frequency-shift infrared thermal sensing, Nano Lett. **13**, 1528 (2013).

[11] T. Yamazaki, S. Ogawa, S. Kumagai, and M. Sasaki, A novel infrared detector using highly nonlinear twisting vibration, Sens. Actuators A **212**, 165 (2014).

[12] T. Ono, H. Wakamatsu, and M. Esashi, Parametrically amplified thermal resonant sensor with pseudo-cooling effect, J. Micromech. Microeng. **15**, 2282 (2005).

[13] S.-J. Kim, T. Ono, and M. Esashi, Thermal imaging with tapping mode using a bimetal oscillator formed at the end of a cantilever, Rev. Sci. Instrum. **80**, 033703 (2009).

[14] J. R. Vig, R. L. Filler, and Y. Kim, Uncooled IR imaging array based on quartz microresonators, J. Microelectromech. Syst. **5**, 131 (1996).

[15] P. Kao and S. Tadigadapa, Micromachined quartz resonator based infrared detector array, Sens. Actuators A **149**, 189 (2009).

[16] M. B. Pisani, K. Ren, P. Kao, and S. Tadigadapa, Application of micromachined Y-cut-quartz bulk acoustic wave resonator for infrared sensing, J. Microelectromech. Syst. **20**, 288 (2011).

[17] Y. Hui and M. Rinaldi, High performance NEMS resonant infrared detector based on an aluminum nitride nanoplate resonator, in *Proceedings of the 17th International Conference on Transducers, Barcelona, Spain* (2013), p. 968, DOI: 10.1109/Transducers.2013.6626930.

[18] W. C. Ang *et al.*, AlN-based piezoelectric resonator for infrared sensing application, in *Proceedings of the IEEE 27th International Conference on Micro Electro Mechanical Systems (MEMS), San Francisco, CA, USA* (2014), p. 688, DOI: 10.1109/MEMSYS.2014.6765734.

[19] V. J. Gokhale and M. Rais-zadeh, Uncooled infrared detectors using gallium nitride on silicon micromechanical resonators, J. Microelectromech. Syst. **23**, 803 (2014).

[20] M. R. Watts *et al.*, Microphotonic thermal detectors and imagers, Proc. SPIE Int. Soc. Opt. Eng. **7194**, 71940T (2009).

[21] J. Zhu, S. K. Ozdemir, and L. Yang, Infrared light detection using a whispering-gallery-mode optical microcavity, Appl. Phys. Lett. **104**, 171114 (2014).

[22] C. T. Nguyen, MEMS technology for timing and frequency control, IEEE Trans. Ultrason. Ferroelectr. Freq. Control, **54**, 251 (2007).

[23] O. Y. Loh and H. D. Espinosa, Nanoelectromechanical contact switches, Nat. Nanotechnol. **7**, 283 (2012).

[24] A. Wong and C. T. Nguyen, Micromechanical mixer-filters ("mixlers"), J. Microelectromech. Syst. **13**, 100 (2004).

[25] D. Rugar, R. Budakian, H. J. Mamin, and B. W. Chui, Single spin detection by magnetic resonance force microscopy, Nature (London) **430**, 329 (2004).

[26] E. Sage, A. Brenac, T. Alava, R. Morel, C. Dupré, M. S. Hanay, M. L. Roukes, L. Duraffourg, C. Masselon, and S. Hentz, Neutral particle mass spectrometry with nanomechanical systems, Nat. Commun. **6**, 6482 (2015).

[27] M. Rinaldi, C. Zuniga, B. Duick, and G. Piazza, Use of a single multiplexed CMOS oscillator as direct frequency read-out for an array of eight AlN contour-mode NEMS resonant sensors, in *Proceedings of the IEEE Sensors*

Conference, Kona, HI, USA (2010), p. 2666, DOI: 10.1109/CSENS.2010.5689874.

[28] M. L. Johnston, I. Kymissis, and K. L. Shepard, FBAR-CMOS oscillator array for mass-sensing applications, IEEE Sens. J. **10**, 1042 (2010).

[29] I. Bargatin, E. B. Myers, J. S. Aldridge, C. Marcoux, P. Brianceau, L. Duraffourg, E. Colinet, S. Hentz, P. Andreucci, and M. L. Roukes, Large-scale integration of nanoelectromechanical systems for gas sensing applications, Nano Lett. **12**, 1269 (2012).

[30] See Supplemental Material at http://link.aps.org/supplemental/10.1103/PhysRevApplied.9.024016 for further details on: fabrication (Appendix A), electromechanical model (Appendix B), noise sources (Appendix C), the detection scheme (Appendix D).

[31] I. Bargatin, E. B. Myers, J. Arlett, B. Gudlewski, and M. L. Roukes, Sensitive detection of nanomechanical motion using piezoresistive signal downmixing, Appl. Phys. Lett. **86**, 133109 (2005).

[32] H. W. C. Postma, I. Kozinsky, A. Husain, and M. L. Roukes, Dynamic range of nanotube- and nanowire-based electromechanical systems, Appl. Phys. Lett. **86**, 223105 (2005).

[33] N. Kacem, S. Baguet, L. Duraffourg, G. Jourdan, R. Dufour, and S. Hentz, Overcoming limitations of nanomechanical resonators with simultaneous resonances, Appl. Phys. Lett. **107**, 073105 (2015).

[34] L. Laurent, J. J. Yon, J. S. Moulet, P. Imperinetti, and L. Duraffourg, Compensation of nonlinear hardening effect in a nanoelectromechanical torsional resonator, Sens. Actuators A **263**, 326 (2017).

[35] R. A. Wood, in *Uncooled Infrared Imaging Arrays and Systems*, edited by W. Kruse and D. D. Skatrud, Semiconductors and Semimetals Series Vol. 47 (Elsevier, New York, 1997), Chap. 3, p. 43.

[36] P. W. Kruse and D. D. Skatrud, *Uncooled Infrared Imaging Arrays and Systems* (Academic Press, New York, 1997), Vol. 47.

[37] A. N. Cleland and M. L. Roukes, Noise processes in nanomechanical resonators, J. Appl. Phys. **92**, 2758 (2002).

[38] W. P. Robins, *Phase Noise in Signal Sources: Theory and Applications* (Peter Peregrinus, Ltd, London, 1984).

[39] D. W. Allan, Statistics of atomic frequency standards, Proc. IEEE **54**, 221 (1966).

[40] M. Sansa *et al.*, Frequency fluctuations in silicon nanoresonators, Nat. Nanotechnol. **11**, 552 (2016).

[41] G. D. Skidmore, C. J. Han, and C. Li, Uncooled microbolometers at DRS and elsewhere through 2013, Proc. SPIE Int. Soc. Opt. Eng. **9100**, 910003 (2014).

[42] A. Holsteen, I. S. Kim, and L. J. Lauhon, Extraordinary dynamic mechanical response of vanadium dioxide nanowires around the insulator to metal phase transition, Nano Lett. **14**, 1898 (2014).

[43] A. Rúa, R. Cabrera, H. Coy, E. Merced, N. Sepúlveda, and F. E. Fernández, Phase transition behavior in microcantilevers coated with M1-phase VO_2 and M2-phase VO_2:Cr thin films, J. Appl. Phys. **111**, 104502 (2012).